Evolution of structural and electronic properties of $TiSe_2$ under high pressure

H. Saqib[1,2] S. Rahman[1], C. Cazorla[3], D. Errandonea[4] Resta Susilo[1], Bin Chen[*1], Ning Dai[*2]

[1]*Center for High Pressure Science and Technology Advanced Research, Shanghai 201203, China*

[2]*Shanghai Institute of Technical Physics, Chinese Academy of Science, Shanghai 201800, China*

[3]*Departament de Física, Universitat Politècnica de Catalunya, Campus Nord B4-B5, Barcelona 08034, Spain*

[4]*Departamento de Física Aplicada-ICMUV, MALTA Consolider Team, Universidad de Valencia, Edificio de Investigación, C/Dr. Moliner 50, Burjassot, 46100 Valencia, Spain*

***Corresponding author: E-mail address:**

chenbin@hpstar.ac.cn (B.C.), &

ndai@mail.sitp.ac.cn (N.D.)

Abstract:

The interplay between the superconductivity and charge-density-wave state in the compressed 1T-$TiSe_2$ is systematically investigated and its structural, optical, and electronic properties are studied. $TiSe_2$ has highly tunable transport properties under pressure, as evident by the pressure-induced metallization, which is confirmed by *ab-initio* calculations. We found several changes in Raman spectra and x-ray diffraction patterns, which demonstrates the occurrence of a first-order structural phase transition from a to at 4 GPa. Additionally, at 16 GPa, the phase spontaneously transforms into a monoclinic phase, and above 24 GPa, the phase returns to the initial phase. Electrical transport results show that metallization occurs above 6 GPa. On top of that, the charge density wave state is suppressed on compression from ambient to 2 GPa, and emerging superconductivity begins at 2.5 GPa, with a critical temperature (Tc) of 2 K. A structural transition accompanies the onset of superconductivity. Superconductivity was observed up to 4 GPa, before vanishing beyond this pressure.

I. INTRODUCTION

Transition metal dichalcogenides (TMDs) have attracted tremendous research interest over the last decade due to their interesting structural chemistry, unusual electronic properties, rich intercalation chemistry as well as wide applications in two-dimensional (2D) devices [1,2]. Phenomena such as the quantum Hall effect, superconductivity, and charge-density-wave (CDW) order have been discovered, stemming from the interplay of various correlations and instabilities in these systems [3-6]. TMDs share the chemical formula MX_2, where M is a transition metal (for instance, Mo, Ti, or W) and X is a chalcogenide atom (S, Se, or Te). Depending on the synthesis technique, the same composition of MX_2 can crystallize in diverse structures with very different electronic properties. Bulk TMDs can be metals such as TaS_2 and $TaSe_2$, semimetals such as $TiSe_2$, semiconductors such as MoS_2, or insulators such as HfS_2. Among TMDs, $TiSe_2$ is very important and has been broadly investigated because of its series of distinctive electronic properties ranging from charge-density wave (CDW) to superconductivity [7-9]. Layered $TiSe_2$, with a band gap (Eg) of 0.18eV, is composed of stacked tri-atomic sheets where each tri-atomic monolayer exhibits a sandwiched structure with a plane of transition metal titanium atoms covalently bonded to and sandwiched between two planes of chalcogen selenium atoms [10] [11,12] [13]. Pure $TiSe_2$ undergoes a commensurate charge-density-wave (CDW) transition below T ~200 K with the formation of a super lattice (2x2x2)[14]. The transition temperature of CDW is enhanced to ~232 K via thinning the sample to nanometers [15].

Owing to its unique structural and electronic properties, $TiSe_2$ has been suggested as a substitute for graphene in thermoelectric applications and a cathode material in batteries [16,17] [3,18,19]. As a very suitable candidate material for optoelectronic applications, research on $TiSe_2$ demands a

significant way to adjust its band gap and electronic properties for the broad-scale use of this 2D material in photoelectric devices. Several recent studies suggest that strain or pressure can provide a clean and controllable way of tuning the band structures and electronic properties of 2D materials. Pressure is considered a powerful tool for manipulating crystal structures, either to tune the structure or physical properties of existing materials or as a route for the preparation of materials with structures unattainable at ambient pressure [20] [21].

Many cases show that the materials' superconducting behavior in the low-pressure region clearly differs from that at high pressures. The superconducting temperature (Tc) was found to be quite sensitive to pressure. There are various cases where the system has re-entered at the superconducting stage at high pressure. In $PdSe_2$, the application of pressure systematically changed the transport properties leading to pressure-induced metallization, and a superconducting state emerged upon the structural transition to the cubic pyrite phase above 6 GPa. A rapid increase in the Tc with compression was observed with a maximum Tc of 13.1 K at ~23 GPa, which is the highest Tc reported in TMDs to date [22]. Such studies motivated us to study $TiSe_2$ under compression for a more complete understanding of its properties.

Both Cu intercalation and the application of pressure in the $TiSe_2$ have led to the suppression of the transition temperature and ultimately the appearance of superconductivity [9,23]. Earlier experimental high-pressure studies on 1T-TiSe2 were limited to 8 GPa, in which the enhancement of T_{CDW} reached a maximum of ~1.1 K at 4GPa [9]. In addition, there is only one reported high-pressure Raman study of this material with a maximum pressure of just 20 GPa [24]. We also found little information about the high-pressure transport properties at room temperature. Thus, it is crucial to carefully explore the high-pressure behavior of 1T-$TiSe_2$ at higher pressures for a thorough understanding of this material. A comprehensive theoretical and experimental analysis

of the structural and physical properties of $TiSe_2$ under high pressure has also never been reported. We have performed the first inclusive study of this vital TMD by combining experimental techniques, including high-pressure XRD, Raman spectroscopy, and transport measurement at room temperature as well as theoretical DFT calculations. We also performed temperature-dependent resistivity measurements at high pressure for the observation of superconductivity. This study will provide the first definitive understanding of the structural changes in the $TiSe_2$ system and its correlation with the transport properties of this material under compression. Our high-pressure X-ray diffraction studies up to 35 GPa show the start of the structural transition from ambient to a after 4 GPa. Then, at about 16 GPa the phase, which spontaneously transits to a phase with the same symmetry as the at 24 GPa. Such re-entrant phase behavior is also confirmed from the density-functional theory calculations. Raman spectroscopy as well as transport measurements confirm the structural changes. The high-pressure phases are found to be metallic. Superconductivity was observed only in a narrow pressure range, i.e. from 2.5 to 4 GPa. The applied pressure effectively enhances conductivity and carrier concentration, which ultimately makes $TiSe_2$ a suitable device for applications in strain-modulated optoelectronic devices.

II. EXPERIMENTAL

Single crystal samples of 1T- $TiSe_2$ used for high-pressure experiments were purchased from HQ Graphene. We performed HP-XRD measurements for 1T- $TiSe_2$ at the Shanghai Synchrotron Radiation Facility (SSRF, BL15U1 beamline), China, with an X-ray wavelength of 0.6199Å. High-pressure conditions were obtained with a diamond-anvil cell (DAC), using silicon oil as a pressure-transmitting medium. Sample pressures were determined using the calibrated ruby pressure standard of Mao et al. [25]. X-ray diffraction patterns were collected using a Mar165

CCD detector. The resulting ring-type diffraction patterns were integrated using the Fit2D software. Le Bail refinement analyses were carried out using the FULLPROF software[26].

Raman spectroscopy experiments were completed using an in Via Renishaw Raman spectrometer system with a laser wavelength of 532 nm and a 2400 g/cm grating. The range of our interest was 100–400 cm^{-1}. Similar to XRD, we used silicon oil as pressure-transmitting media during measurements under HP. The wavenumbers of the Raman peaks were determined with an accuracy of 1 cm^{-1}. High-pressure electrical resistivity measurements were performed using the standard four-probe technique in a DAC up to 35 GPa. The gasket was insulated with a mixture of epoxy and cubic boron nitride. Four platinum leads were arranged to contact the sample in the chamber. No pressure medium was used for the resistivity measurement. The resistance was determined by the Van der Pauw method[27].

First-principles calculations based on density functional theory (DFT)[28] were performed to theoretically analyze the structural, vibrational, and electronic properties of $TiSe_2$ under pressure. The meta-GGA SCAN exchange-correlation functional [29] was employed for most calculations as it is implemented in the VASP package [30].The “projector augmented wave” method was employed to represent the ionic cores[31] and we considered the following electrons as valence: Ti's 3*d* and 4*s* and Se's 4*s* and 4*p*. Wave functions were represented in a plane-wave basis truncated at 650 eV, and for integrations within the first Brillouin zone, a Gamma-centred **k**-point grid of 14x16x10 was employed. Geometry relaxations were performed by imposing a tolerance on the atomic forces of 0.005 $eV \cdot Å^{-1}$. By using these technical parameters, the obtained energies were converged to within 0.5 meV per formula unit.

Zero-temperature phonon frequencies were estimated with the small-displacement method, in which the force-constant matrix is calculated in real space by considering the proportionality between atomic displacements and forces [32] The quantities that our phonon calculations need to converge with include the size of the supercell, the size of the atomic displacements, and the numerical accuracy in the sampling of the Brillouin zone. We found the following settings to provide quasi-harmonic free energies converged to within 5 meV per formula unit: 4×4×4 supercells (the figures indicate the number of unit cell replicas along the corresponding lattice vectors), atomic displacements of 0.02 Å, and $\boldsymbol{q}$-point grids of 16×16×16. The value of the phonon frequencies, ω_{qs}, was obtained with the PHON code developed by Alfè [33] .Using this software, we exploited the translational invariance of the system to impose the three acoustic branches to be exactly zero at the centre of the Brillouin zone and applied central differences in the atomic forces.

III. RESULTS & DISCUSSION

A. Pressure-induced structural changes from X-ray diffraction

To explore the thermodynamic stability of pristine 1T-$TiSe_2$ under high pressure, we performed synchrotron XRD measurements at room temperature up to 30.0 GPa, as shown in Fig.1. Due to the strong preferred orientation of the compressed sample, all XRD patterns were analyzed using the Le Bail method.

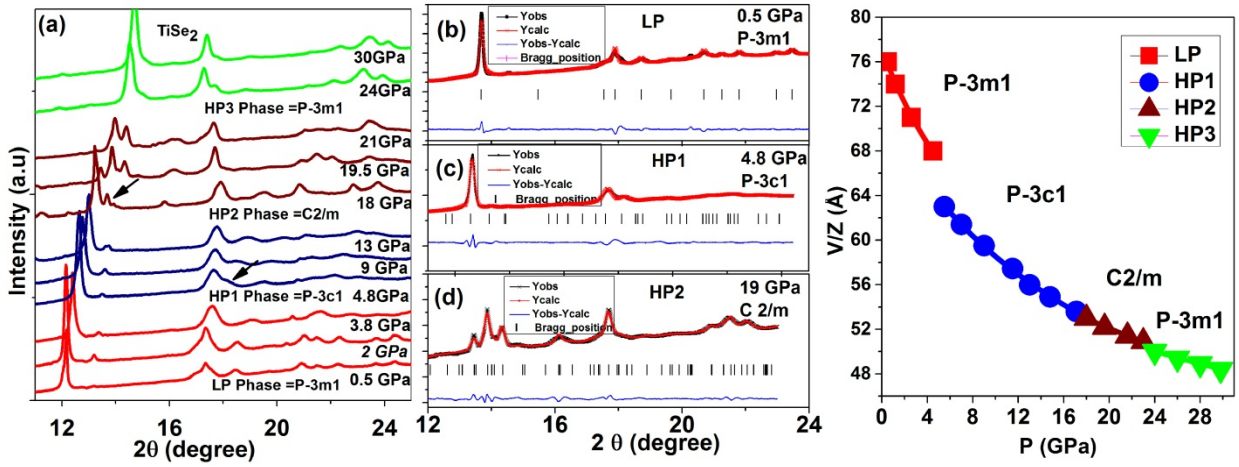

Figure1. (a) Angle dispersive XRD patterns for $TiSe_2$ at selected pressures at room temperature (λ = 0.4959 Å). Arrows indicate the appearance of new peaks. High-pressure x-ray diffraction patterns of $TiSe_2$ at room temperature (λ = 0.6199 Å). (b-d) Le Bail refinements for the low-pressure and new HP1, HP2 phases at 0.5 GPa, 5.5 GPa, and 19 GPa, respectively. (e) Unit cell volume as a function of pressure for different phases.

Pristine 1T-$TiSe_2$ crystallizes in a trigonal structure with the space group at ambient pressure. Under compression up to 3 GPa, there was no major change found in the XRD patterns except a gradual shift of the Bragg peaks towards higher angles, and all patterns were identified with the phase, as shown in Fig 1(b). The Le Bail analysis of powder XRD patterns at 0.5 GPa indicates the pure trigonal phase, as shown in Fig 1(b). The resulting lattice parameter are a=b= 4.210 Å, c = 4.974 Å, with profile-matching parameters RP = 1.86 %, RWP = 1.23 %, $\chi 2$ = 1.4, which are in good agreement with the previous report [13].

Beyond 3.5 GPa, extra diffraction peaks indicated by arrows start to appear, suggesting the onset of a structural phase transition. Finally, at around 4 GPa we observed a structural phase transition from the to a phase. Representative Le Bail refinements of the HP-XRD patterns at 5.5 GPa are illustrated in Fig. 1(c). Interestingly, at about 16 GPa the phase spontaneously transits to the

phase, as shown in Fig 1(d). This phase returns to the ambient phase after 24 GPa, as shown in Fig S3. Thephase stabilizes again up to the highest pressure we attained in our study. Our theoretical calculations also predicted the existence of a - - - structural phase sequence.

From the experiments, we determined the pressure dependence of the volume for different phases. Discontinuities in the volume indicate that the first and third transitions are first-order transformations. In the second transition, there is no detectable volume discontinuity. As is a maximal subgroup of , the second transition could have a second-order nature. The unit-cell volume as a function of pressure was fitted with the following third-order Birch-Murnaghan equation of state [34,35]:

(1)

where P and V are the measured pressure and unit cell volume, respectively. K_0 is the bulk modulus, K'_0 is the first pressure derivative of the bulk modulus, and V_0 is the unit cell volume at ambient conditions. The fits give K_0 = 31(4) GPa, K'_0 = 4.0, V_0 =78(5) Å^3, for the LP trigonal phase, K_0 = 33(5) GPa, K'_0 = 4.0, for the HP-1 trigonal phase, and K_0 = 41(5) GPa, K'_0 = 4.0, for the HP-2 monoclinic phase while K_0 = 47(4) GPa, and K'_0 = 4.0 for the HP-4 phase trigonal phase, where P and V are the measured pressure and unit cell volume, respectively, as shown in the Fig 1(e).

The profile matching parameters and lattice constant parameters of both low-pressure and high-pressure phases (HP-1, HP-2) obtained from the profile Le Bail refinements are given in Fig. 1 (b-d) and Table 1. The Le Bail fit for the HP3 phase is shown in Fig. S1. On releasing pressure to ambient, the original ambient phase is recovered. Hence, the phase transition is confirmed to be reversible.

Table 1: Lattice parameters and profile matching parameters of the cubic and the high-pressure phases

Phase	***P***	**Lattice constant parameters**			**Profile matching parameters**		
		A	*B*	*C*	R_p	R_{wp}	χ^2
Trigonal	0.5 GPa	4.210763 (1) Å	4.210763 (1) Å	4.974298 (1) Å	1.18%	1.41%	0.97
Trigonal	5.5 GPa	7.044479 (2) Å	7.044479 (2) Å	11.32984 7 (2) Å	1.41%	1.78%	1.62
Monoclinic	19 GPa	17.562742 (3) Å	3.276016 (3) Å	5.426599 (3) Å	1.80%	1.93%	1.89
Trigonal	24 GPa	3.08760 (3) Å	3.08760 (3) Å	6.11930 (3) Å	1.30%	1.33%	1.32

To obtain a deeper insight into the nature of the structural changes found in our experimental results, we performed first-principles density functional theory (DFT) calculations. The enthalpy curves computed for bulk $TiSe_2$ are shown in Fig. 2(a). It can be appreciated that the stable phase from ambient pressure up to ≈ 3.4 GPa is the hexagonal . At larger pressures, the crystal is stabilized in the hexagonal phase, which subsequently transforms spontaneously (i.e., in a continuous second-order fashion) into the monoclinic *C2/m* phase at a theoretical pressure of 11.2 GPa. This space group is a subgroup of and the enthalpy differences between the two phases are very small in comparison to the differences with the enthalpy of the phase. The monoclinic *C2/m* phase subsequently transforms into the hexagonal phase at a theoretical pressure of 15.8 GPa, when the former structure becomes vibrationally unstable. Thus, the monoclinic *C2/m* phase appears to act as a structural bridge between the hexagonal phases and . Therefore, the reentrant phase behavior observed in the experiments is fully confirmed by the theoretical enthalpy curves shown in Fig. 2(a). However, we appreciate that the DFT calculations tend to systematically underestimate the experimental transition pressures, This is probably due to neglecting temperature effects and dispersion long-range interactions in the simulations.

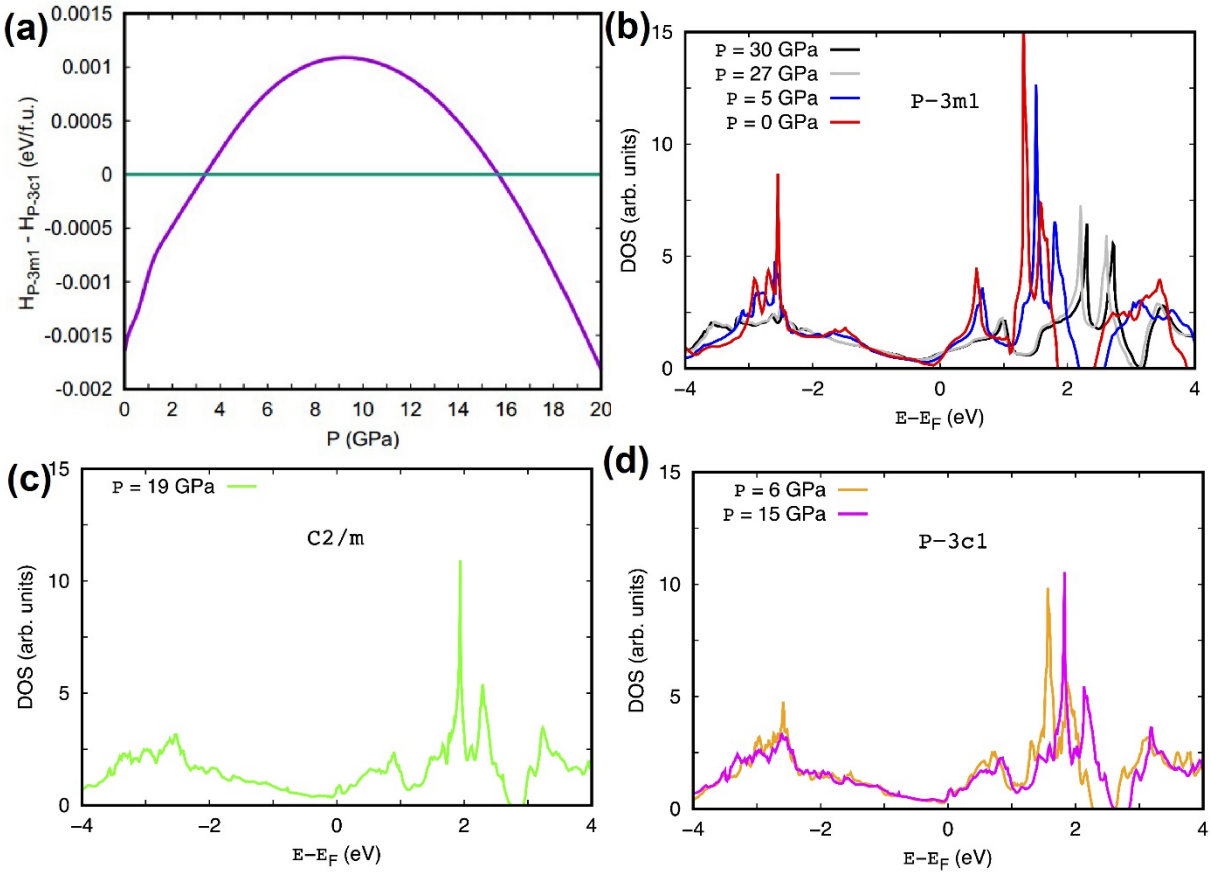

Fig 2(a). Enthalpy curves are estimated with density functional theory (DFT) techniques and expressed as a function of pressure. The narrow pressure range in which the stable structure is the monoclinic C2/m phase, namely, $11.2 \leq P \leq 13.8$ GPa, is not indicated in the figure. (b-d) Calculated density of electronic states for bulk $TiSe_2$ at several pressures and for different crystal structures.

Pressure-dependent Raman spectroscopy

Raman spectroscopy is a sensitive technique for detecting subtle structural changes and chemical reactivity. Therefore, it is suitable to shed light on the observed phase transitions in $TiSe_2$. A Raman spectroscopy measurement under pressure was employed up to 30 GPa, as shown in Fig 3(a).The group-theoretical analysis for 1T-$TiSe_2$ predicts the presence of nine zone-center

vibrational modes $A_{1g} + 2A_{2u} + 2E_u + E_g$ [36]. The degenerated E_g mode and the A_{1g} mode are Raman active, while one degenerated E_u and one A_{2u} mode are IR-active modes. The remaining modes are acoustics modes. The Raman-active A_{1g} mode arises due to the out-of-plane vibration of the stretching of two Se atoms moving relative to one another along the z-axis, while the E_g mode represents the symmetric in-plane bending of the Se atoms along the xy directions.

3

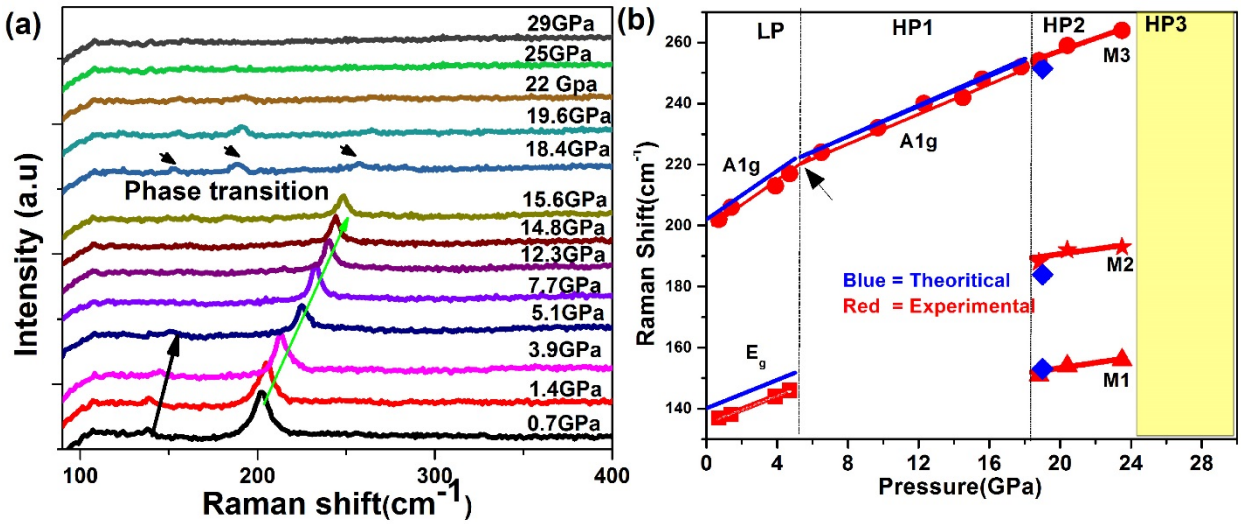

Figure 3(a). Raman spectra of $TiSe_2$ from 0-25 GPa showing the Raman mode disappearing at the first phase transition (around 5.5GPa). (b) A comparison between the experimental and calculated modes' frequencies.

We calculated the Raman- and IR-active phonon frequencies and also phonon dispersions, which are shown, as an example for the and phase, in the Sup. Material (Fig. S4) showing their dynamical stability. The calculated Raman frequencies will be used to assign the mode symmetry of measured Raman modes. Based on our theoretical calculations and the existing literature, the peaks obtained for the ambient spectrum at around 137 cm^{-1} and 202 cm^{-1} are assigned to the E_g

and A_{1g} modes, respectively. These results are similar to the previous studies at ambient conditions [37].

Our LP phase results are similar to Rajaji et al, however, they were unable to explore the Raman measurements at higher pressure [24]. We also confirmed our experimental results by theoretical analysis, as discussed later in this section.

As the pressure increases, the intensity of the A_{1g} and E_g mode decreases along with the gradual shift towards higher frequencies. With compression, the peak intensity of the Eg mode reduces rapidly and completely disappears above 5 GPa. This mode has very little intensity from the beginning of the experiment. Thus, with the further reduction of intensity, it was not possible to follow the Eg mode above ~6 GPa. This disappearance of Eg mode is indicative of the first phase transition. Our structural analysis through XRD also indicates the first phase transition in this pressure range.

Our DFT calculations proposed various modes for the first high-pressure (HP1) phase. This phase has $5A_{1g}$ and 12_{Eg} Raman active modes, while there are 17 Infrared active modes, including $6A_{2u}$ and $11E_u$ modes. Owing to the low scattering factor and the reduced thickness of the sample, we only observed the strongest A_{1g} mode in our experiment.

Figure 3(a) shows the three new modes (M1, M2, and M3) that appear above 16 GPa represent another phase transition (labeled as HP2), as corroborated by our XRD studies. The increase in the number of modes is consistent with the occurrence of the HP1-HP2 transition. Our theoretical calculations predicted the presence of the following modes for the second HP2 phase:

Raman active modes: 4Ag + 2Bg

Infrared active modes: 3Au + 6Bu

We observed three of the six Raman modes mentioned above. According to our performed DFT calculations, the phase is found to be stable in a small pressure range of around 4.6 GPa so we have the phonons for this phase at only one pressure value. Good agreement exists between the observed and calculated Raman modes, as shown in Figure 3(b). All the Raman modes disappear by increasing the pressure beyond 24 GPa, which signposts the phase transition. Our XRD experiments also indicate the presence of a phase transition beyond 24 GPa.

In general, when pressure increases, we observe a monotonous increase (hardening) in Raman frequencies. Any deviation in this suggests changes in the structure or electronic properties of the material. In our case, all the modes seem to harden with increasing pressure, as expected. Nevertheless, there are distinct changes in the evolution of Raman frequencies as a function of pressure, which are important to signify transitions in the 1T-$TiSe_2$ system.

There are subtle changes in the pressure dependence of the A_{1g} mode frequency, which is the most intense Raman peak of 1T- $TiSe_2$ (low-pressure phase) and the HP phase. By using the linear fit equation $\omega(P) = \omega(P0) + a1(P-P0)$ to determine the slope ($a1 = d\omega/dP$) of the A1g mode frequency in Figure 2(a), we observe a distinct change in slopes in the pressure at ~6 GPa. Such changes in the slope, and the disappearance of the E_g mode of the low-pressure phase, point towards the structural change.

Table 2:Calculated and experimental Raman modes with corresponding dw/dP and mode Grüneisen parameters.

Low-pressure phase LP	**High-pressure phase 1 HP1**	**High-pressure phase 2**

								HP2			
Raman modes Experimental $_0$ (cm^{-1})	**Raman modes Calculated $_0$ (cm^{-1})**	**d /dP (cm^{-1}/GPa)**		**Raman modes $_0$ (cm^{-1})**	**Raman modes Calculated $_0$ (cm^{-1})**	**d /dP (cm^{-1}/GPa)**		**Raman modes $_0$(cm^{-1})**	**Raman modes Calculated $_0$ (cm^{-1})**	**d /dP (cm^{-1}/GPa)**	
139.2	140	1.86	0.45	210	139.2	1.12	0.5	212	210	1.12	0.5
201	200	2.97, 2.64	0.36					180	183	1.05	0.38
								145	143	1.7	0.42

The mode frequencies of all the observed Raman modes, pressure coefficients and calculated Grüneisen parameters are shown in Table 2. The mode-Grüneisen parameters (γ) were obtained for the LP, HP1 and HP2 phases with the equation: $\gamma = K0/\omega_0(d\omega/dP)$ by using the bulk modulus (K0) determined from x-ray diffraction data. The values of the Grüneisen parameters for the LP, HP1, and HP2 ranged from 0.36–0.45, 0.5, and 0.38–0.5, respectively. The obtained mode Grüneisen parameters can be used to determine the heat capacities and vibrational entropies using the Kieffer model.[38]

D . Pressure-induced superconductivity

The layered 1T- $TiSe_2$ is a semimetal with an indirect band gap of 0.18 eV where the different layers are interconnected through a van der Waals interaction and can be exfoliated into atomically thin layers. Note that our DFT calculations predict a metallic ground state for $TiSe_2$ within the entire range of investigated pressures, see Figs.2(b)-(d); this outcome indicates that our first-principles calculations tend to underestimate the small energy band gap of $TiSe_2$, which is a well-known drawback of standard DFT approaches. Here, we present the effect of pressure on the evolution of the electronic behavior of this material. Figure 4(a) shows our new finding of resistivity as a function of pressure.

The pressure-dependent resistivity of $TiSe_2$ was obtained up to 40 GPa. Fig. 4(a) depicts the electrical resistivity (ρ) of $TiSe_2$ as a function of P at room temperature. Pressure-dependent room-temperature electrical resistivity on $TiSe_2$ reveals a sharp decrease in resistivity from ambient pressure to about 4 GPa. Such a sharp drop in this resistivity may be due to the structural phase transition indicated by our XRD measurement. With further compression, the resistivity shows a gradual decrease up to 13 GPa, after which it became almost pressure-independent for the region 12 GPa < P < 20 GPa. Our HP XRD and Raman spectroscopy results both show a second structural phase transition in this region.

The resistivity of the high-pressure monoclinic phase is smaller than that of the low-pressure trigonal phase. At low pressure of about 4.5 GPa the resistivity sharply decreases to a minimum. Our HP–XRD results confirmed that the ambient trigonal phase began transforming to the trigonal phase at this pressure.

The extremely low resistivity in the HP2 region after 24 GPa exhibits a typical metallic behavior. Above 25 GPa, the change of resistance is negligible, and it becomes/remains almost pressure independent with the further rise in pressure. The order of magnitude of the electrical resistivity of low-pressure trigonal phase and monoclinic high-pressure phase at ambient temperature changes from R=0.5 Ω to R=0.04 Ω and from R=0.5 Ω to R=0.03 Ω, respectively. The reduction in bond distances might be one reason for these changes.

The sample was decompressed by gradually decreasing the pressure. Complete decompression results in a relatively higher initial value of resistivity than the ambient phase, which may be due to some defect after decompression from the HP phase.

In order to achieve a more comprehensive understanding of the electrical properties, we measured the temperature-dependent resistivity further from 0.7 GPa up to 2.2GPa, as shown in Fig 4(b). The resistivity curves up to 1.1 GPa are similar to those at ambient pressure. The sharp curvature in resistivity is indicative of the CDW transition. $TiSe_2$ was one of the first known CDW-bearing compounds and is also one of the most frequently studied, although the nature of its CDW transition has been controversial for decades. In our case, the CDW transition temperature, T_{CDW}, identified from the maximum of $-d\rho(T)/dT$, gradually shifts to a lower temperature with compression. At the same time, the resistivity anomalies that correspond to the CDW transition are weakened with increasing pressure. It is clearly shown that the application of pressure suppresses the phase transition and that the associated resistivity anomaly becomes much less prominent. In this pressure range, the resistivity above the transition represents weak nonmetallic temperature dependence. At temperatures well below the transition, the electrons uncondensed into the CDW give a metallic character to the resistivity. There are various cases where CDW transitions ultimately lead to the appearance of superconductivity.

Further application of pressure gives rise to the metallic high-temperature region where the resistivity behaves linearly with temperature. At the same time, we observed a monotonous decrease in the CDW transition temperature that ultimately becomes difficult to identify above 2.5 GPa, and disappears completely above 3 GPa from our resistivity measurements. In the pressure range of 2-4 GPa, we observed superconductivity at low temperature, where Tc = 1 K at 3 GPa, then increases slightly to 1.5 K at 3.5 GPa.

Based on theoretical studies by Koley et al., the preformed excitons in normal state $TiSe_2$ drive the compound to undergo a CDW superconducting phase transition under pressure.[39]

This indicates the influence of pressure on the transition is not primarily through the change in the size and shape of the Fermi surface but must be through the stiffening of the lattice force constants. It was suggested that the pressure dependence of the transition is stronger than that expected from the Fermi-surface changes alone, and hence, the phonon-driven model by White and Lucovsky can be favored for the structural distortion in $TiSe_2$.[40].

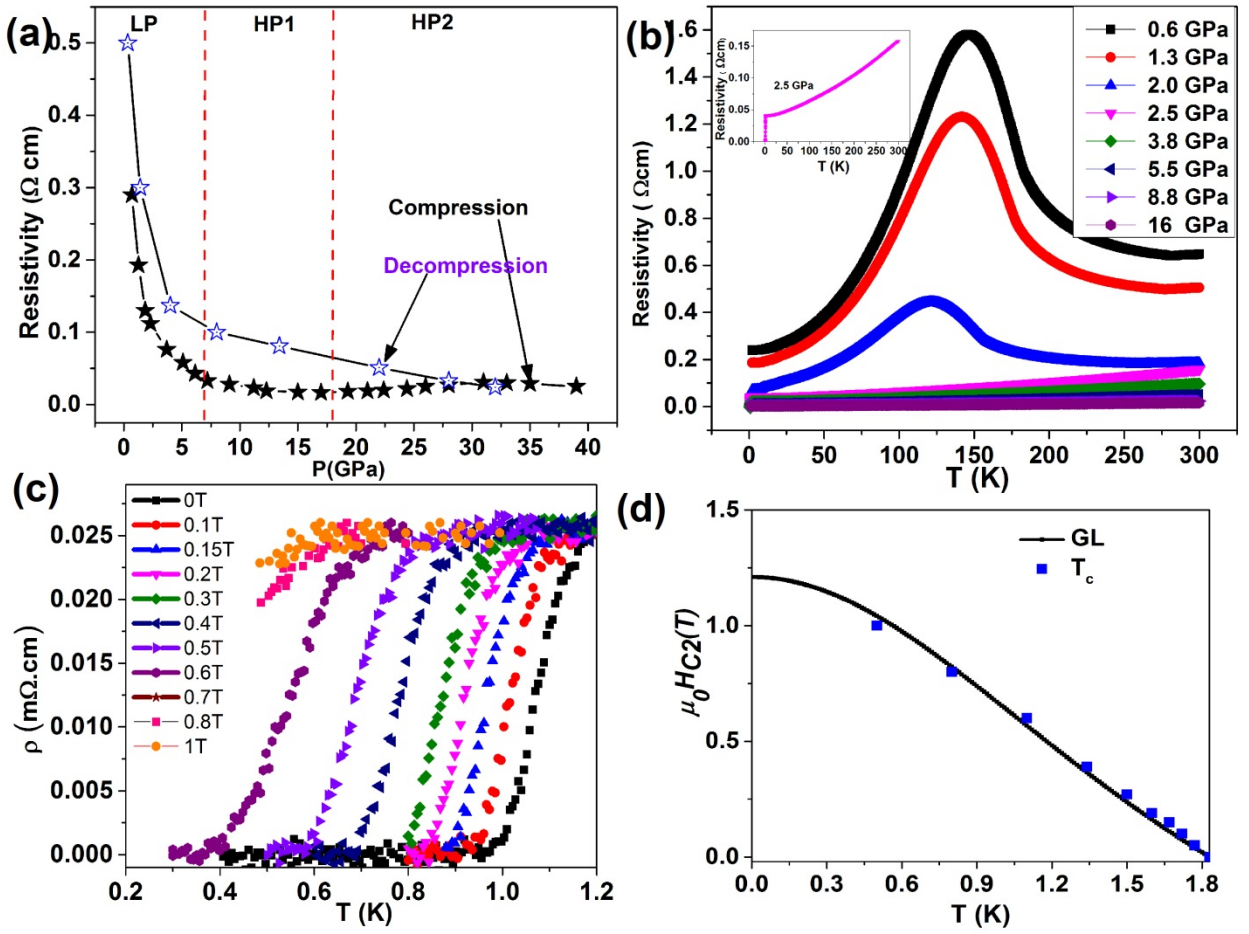

Fig4. Electrical resistance behavior of $TiSe_2$ as a function of pressure at RT. (b) Temperature-resistivity curves at different pressures. (c). Temperature dependence of resistivity under different magnetic fields at 3.8GPa. (d) $\mu_0 H_{c2}$-T phase diagram, where the solid line represents fitting by the GL equation.

In order to confirm the appearance of SC in the compressed TiSe2, we performed resistivity measurements under different applied magnetic fields at 3.8 GPa, as shown in Figure 4(c). Superconductivity in pure 1T-TiSe2 is highly sensitive to the magnetic field, which is in sharp contrast to the Cu intercalated system Cu_xTiSe_2 [9,23]. Zero resistance at 3.8 GPa gradually lifts as the applied magnetic field increases. Simultaneously, the Tc decreases towards low temperature and the superconducting transition is gradually suppressed by the increasing magnetic field.

In Fig. 4(d), we show the upper critical field, Hc2, determined from the onset of the resistivity drop. The Hc2 vs. Tc curve was then fitted with the empirical expression based on the Ginzburg-Landau (GL) theory (e.g. [41]) which takes the form of:

The data in Figure 4(b) can be well-fitted using the above equation. The value of at 3.8 GPa is determined to be 1.22 T. This value is smaller than the value of TiTe2, e.g. >10 T [42], but higher than the BCS Pauli limit of 2.8 T.

E. Discussion

Pressure or compressive strain is known to be a powerful and clean way for continuously tuning the crystal and electronic structures in TMDs. Due to the weak interlayer van der Waals interaction, the interlayer van der Waals bonding in 2D TMD is highly compressible. Therefore, it can be expected that pressure or compressive strain will introduce a dramatic shortening of this interlayer bonding, thereby enhancing the electronic interactions between the layers. Our XRD experiment illustrates a phase transition from a trigonal to a phase that ultimately changes to a monoclinic phase at 5 and 16 GPa, respectively. We observed a reentrant phase behavior where

the phase transits back to the original phase. We confirmed the reliability of the occurrence of such a transition sequence under pressure through DFT calculations.

A phase diagram of 1T-TiSe2 summarizes all the results under non-hydrostatic compressions (Fig 5). The CDW is seen in a pressure range from ambient to 2 GPa, where our XRD data did not show any structural change in this pressure range. Our Raman measurements also did not point towards any structural transition in this region. Gradual shifting in the peak is merely due to compression. Therefore, we can conclude that the CDW transition does not effect the structural properties of $TiSe_2$. From 2 GPa to 4 GPa, superconductivity is observed. Our Raman and XRD measurements indicate the presence of a first-order structural phase transition. Similarly Transport measurements also show a rapid decrease in the resistivity for this pressure region after 4 GPa. Slight difference in pressure points may be due to the non-hydrostatic conditions in the transport measurements. Similarly after 16 GPa, another phase transition is observed from the XRD and Raman measurements. The reentrant phase behavior is seen in the XRD measurements.

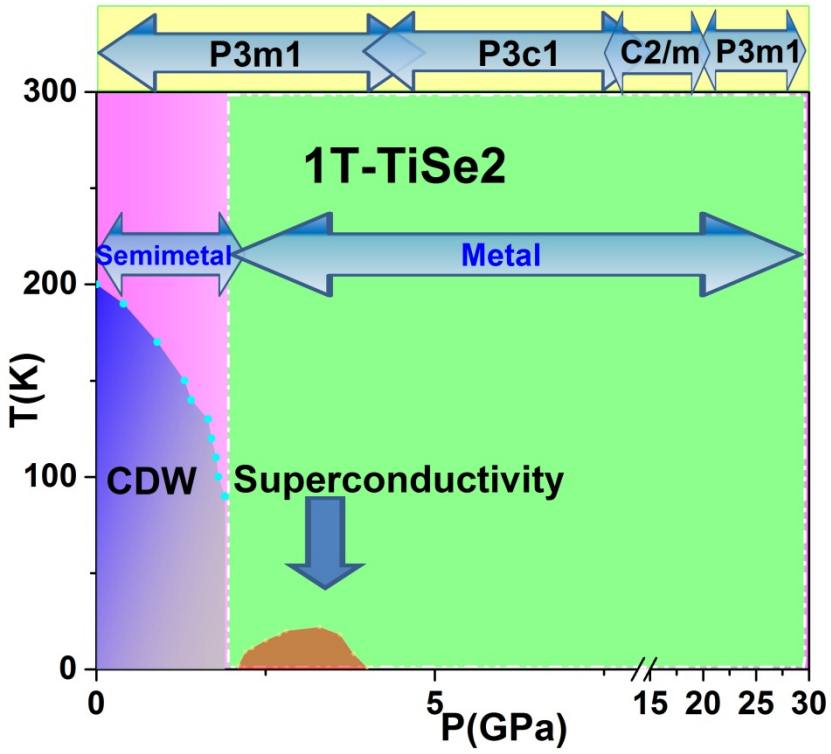

Fig.5 The phase diagram for 1T-TiSe2

Lattice instability and structural fluctuation have been generally observed in TMDs through X-ray diffraction, electron diffraction, and temperature-dependent resistivity measurements, suggesting a close connection between the lattice degrees of freedom and superconductivity. There are various studies on TMDs where superconductivity has been associated with a structural phase transition. Chi et al. investigated the crystal structure and electrical resistivity of 2Hc-MoS_2 under pressure up to 160 GPa and observed a pressure-induced 2Hc-to-2Ha polytype transformation near 30 GPa accompanied by a semiconductor-to-metal transition.[43] The 2Ha phase exhibited superconductivity at pressures beyond 90 GPa. A dramatic increase of the Tc was observed from 5 K to 12 K. There are various other examples where the emergence of superconductivity is associated with the structural phase transition. $ZrTe_5$ clearly reveals the semimetal to superconductor transition at around 6 GPa, which is related to the phase transition

from Cmcm to C2/m.[43] Unlike MoS_2, $MoTe_2$ exhibits a semiconductor-to-metallic transition by the gradual tuning of the electric structure and band gap without a structural transition[44]. In our current work, superconductivity emerges in $TiSe_2$ as the CDW transition is suppressed above ~2 GPa. Interestingly superconductivity only appears in a narrow pressure region, i.e., between 2 – 4 GPa. Our XRD data reveals a structural phase transition from the trigonal to trigonal above 4 GPa, which suggests that the pressure-induced superconductivity in $TiSe_2$ appears in the phase. In an isostructural TiTe2, the superconductivity emerges together with the formation of the high-pressure monoclinic C2/m phase [42]. By comparison, the structural transition to the phase above 4 GPa destroys the superconductivity in $TiSe_2$, which indicates that this phase is unfavorable for hosting superconductivity. We observed that the pressure derivative of the $TiSe_2$ CDW transition temperature is negative, like the similar experimental observation by Kumara et al. [9].

The CDW fluctuations are tightly linked with superconductivity in 1T-$TiSe_2$. This behavior is similar to that of several families of materials where the superconducting dome has been discovered in the vicinity of the purely electronic-ordered phase, addressing the quantum critical point strengthens the viewpoint of excitonic superconductivity in 1T-$TiSe_2$ [45,46]. On the other hand, the continuous development of the soft phonon mode in the vicinity of the CDW transition, both in Cu-intercalated and pure and pressurized material,[9] suggests that the lattice deformation may not be regarded as a secondary effect that simply follows the electronic ordering.

The transition is ascribed to the Se 4p and Ti 3d bands inversion with different parity at the C-point. It is very likely that the pressure range where the topologically nontrivial phase emerges likely overlaps with the state where the superconductivity emerges, which might lead to a self-

induced topological surface superconductivity in pressurized 1T-$TiSe_2$. However, in our studies, we also observed the superconductivity transition is related to the structural phase transition too.

Conclusions:

In conclusion, $TiSe_2$ undergoes a pressure-induced phase transition from the to a phase near 4 GPa, and at about 16 GPa the phase changes to a phase. Interestingly, this transits back to the original which stabilizes again up to 35 GPa; the highest pressure reached in our study. Such reentrant phase behavior was carefully studied through Raman and transport measurements. Metallic behavior was determined for the three high-pressure phases through the temperature dependent resistivity and *ab initio* calculations. Superconductivity was observed in the sample at 2.5 GPa. The extensive and continuous tuning of its electronic structure can be potentially used for energy-variable (IR-visible) optoelectronics and photovoltaics applications.

Acknowledgments

D. E. acknowledges the financial support given by the Spanish Ministry of Science, Innovation and Universities under Grant Nos. PID2019-106383GB-C41 and RED2018-102612-T (MALTA Consolider-Team network) and by the Generalitat Valenciana under Grant Prometeo/2018/123 (EFIMAT). C.C. acknowledges support from the Spanish Ministry of Science, Innovation, and Universities under the "Ramon y Cajal" fellowship RYC2018-024947-I.

REFERENCES:

[1] M. N. Ali *et al.*, Nature **514**, 205 (2014).
[2] I. Pletikosić, M. N. Ali, A. V. Fedorov, R. J. Cava, and T. Valla, Phys. Rev. Lett. **113**, 216601 (2014).
[3] J. A. Wilson, F. J. Di Salvo, and S. Mahajan, Advances in Physics **24**, 117 (1975).
[4] E. Revolinsky, E. P. Lautenschlager, and C. H. Armitage, Solid State Communications **1**, 59 (1963).
[5] A. P. Nayak *et al.*, Nature Communications **5**, 3731 (2014).
[6] Y. Liu, R. Ang, W. J. Lu, W. H. Song, L. J. Li, and Y. P. Sun, Applied Physics Letters **102**, 192602 (2013).

[7] C. Berthier, P. Molinié, and D. Jérome, Solid State Communications **18**, 1393 (1976).
[8] A. Zunger and A. J. Freeman, Physical Review B **17**, 1839 (1978).
[9] A. F. Kusmartseva, B. Sipos, H. Berger, L. Forró, and E. Tutiš, Physical Review Letters **103**, 236401 (2009).
[10] Q. Zhang, Y. Cheng, and U. Schwingenschlögl, Scientific Reports **5**, 8379 (2015).
[11] G. A. Wiegers, Progress in Solid State Chemistry **24**, 1 (1996).
[12] A. H. Thompson, Solid State Communications **17**, 1115 (1975).
[13] C. Riekel, Journal of Solid State Chemistry **17**, 389 (1976).
[14] P. Chen, Y. H. Chan, X. Y. Fang, Y. Zhang, M. Y. Chou, S. K. Mo, Z. Hussain, A. V. Fedorov, and T. C. Chiang, Nature Communications **6**, 8943 (2015).
[15] D. L. Duong, G. Ryu, A. Hoyer, C. Lin, M. Burghard, and K. Kern, ACS Nano **11**, 1034 (2017).
[16] R. Bhatt *et al.*, Journal of Applied Physics **114**, 114509 (2013).
[17] Y. Gu, Y. Katsura, T. Yoshino, H. Takagi, and K. Taniguchi, Scientific Reports **5**, 12486 (2015).
[18] L. Fu, C. L. Kane, and E. J. Mele, Physical Review Letters **98**, 106803 (2007).
[19] Y. I. Joe *et al.*, Nature Physics **10**, 421 (2014).
[20] D. Machon, F. Meersman, M. C. Wilding, M. Wilson, and P. F. McMillan, Progress in Materials Science **61**, 216 (2014).
[21] M. Maczka, A. G. Souza Filho, W. Paraguassu, P. T. C. Freire, J. Mendes Filho, and J. Hanuza, Progress in Materials Science **57**, 1335 (2012).
[22] M. A. ElGhazali, P. G. Naumov, Q. Mu, V. Süß, A. O. Baskakov, C. Felser, and S. A. Medvedev, Physical Review B **100**, 014507 (2019).
[23] E. Morosan, H. W. Zandbergen, B. S. Dennis, J. W. G. Bos, Y. Onose, T. Klimczuk, A. P. Ramirez, N. P. Ong, and R. J. Cava, Nature Physics **2**, 544 (2006).
[24] V. Rajaji, S. Janaky, S. C. Sarma, S. C. Peter, and C. Narayana, Journal of Physics: Condensed Matter **31**, 165401 (2019).
[25] H. Mao, J.-A. Xu, and P. Bell, J. Geophys. Res. Solid Earth **91**, 4673 (1986).
[26] J. Rodríguez-Carvajal, Physica B: Condensed Matter **192**, 55 (1993).
[27] D. Errandonea, A. Segura, D. Martínez-García, and V. Muñoz-San Jose, Physical Review B **79**, 125203 (2009).
[28] S. Azaele, S. Suweis, J. Grilli, I. Volkov, J. R. Banavar, and A. Maritan, Reviews of Modern Physics **88**, 035003 (2016).
[29] J. Sun, A. Ruzsinszky, and J. P. Perdew, Physical Review Letters **115**, 036402 (2015).
[30] G. Kresse and J. Furthmüller, Physical Review B **54**, 11169 (1996).
[31] P. E. Blöchl, Physical Review B **50**, 17953 (1994).
[32] C. Cazorla, D. Errandonea, and E. Sola, Physical Review B **80**, 064105 (2009).
[33] D. Alfè, Computer Physics Communications **180**, 2622 (2009).
[34] E. Greenberg, G. K. Rozenberg, W. Xu, R. Arielly, M. P. Pasternak, A. Melchior, G. Garbarino, and L. S. Dubrovinsky, High Pressure Research **29**, 764 (2009).
[35] S. Rahman *et al.*, Physical Review B **97**, 174102 (2018).
[36] H. Ding and B. Xu, The Journal of Chemical Physics **137**, 224509 (2012).
[37] S. Sugai, K. Murase, S. Uchida, and S. Tanaka, Solid State Communications **35**, 433 (1980).
[38] S. W. Kieffer, Reviews of Geophysics **17**, 20 (1979).
[39] S. Koley, Solid State Communications **251**, 23 (2017).
[40] R. H. Friend, D. Jerome, and A. D. Yoffe, Journal of Physics C: Solid State Physics **15**, 2183 (1982).
[41] L. Fang, Y. Wang, P. Y. Zou, L. Tang, Z. Xu, H. Chen, C. Dong, L. Shan, and H. H. Wen, Phys. Rev. B **72**, 014534 (2005).
[42] U. Dutta, P. S. Malavi, S. Sahoo, B. Joseph, and S. Karmakar, Physical Review B **97**, 060503 (2018).

[43] Z. Chi *et al.*, Physical Review Letters **120**, 037002 (2018).
[44] X.-M. Zhao, H.-y. Liu, A. F. Goncharov, Z.-W. Zhao, V. V. Struzhkin, H.-K. Mao, A. G. Gavriliuk, and X.-J. Chen, Physical Review B **99**, 024111 (2019).
[45] V. A. Sidorov, M. Nicklas, P. G. Pagliuso, J. L. Sarrao, Y. Bang, A. V. Balatsky, and J. D. Thompson, Physical Review Letters **89**, 157004 (2002).
[46] J. Wosnitza, Journal of Low Temperature Physics **146**, 641 (2007).